IEEE Access
Multidisciplinary ⋮ Rapid Review ⋮ Open Access Journal

Received January 5, 2020, accepted February 5, 2020, date of publication February 11, 2020, date of current version February 24, 2020.

Digital Object Identifier 10.1109/ACCESS.2020.2973187

Optimizing Linearity and Sensitivity of 3D-Printed Diaphragms With Chirped FBGs in CYTOP Fibers

ARNALDO G. LEAL-JUNIOR[1,2], (Member, IEEE), HELDER R. O. ROCHA[2], ANTREAS THEODOSIOU[3], (Member, IEEE), ANSELMO FRIZERA[2], (Member, IEEE), CARLOS MARQUES[4], KYRIACOS KALLI[3], (Senior Member, IEEE), AND MOISÉS R. N. RIBEIRO[2]

[1]Mechanical Engineering Department, Federal University of Espirito Santo, Vitória 29075-910, Brazil
[2]Graduate Program in Electrical Engineering, Federal University of Espirito Santo, Vitória 29075-910, Brazil
[3]Photonics and Optical Sensors Research Laboratory, Cyprus University of Technology, 3036 Limassol, Cyprus
[4]I3N & Physics Department, Universidade de Aveiro, Campus Universitário de Santiago, 3810-193 Aveiro, Portugal

Corresponding author: Arnaldo G. Leal-Junior (leal-junior.arnaldo@ieee.org)

This work was supported by the Fundação de Amparo à Pesquisa e Inovação do Espírito Santo (FAPES) under Grant 85426300 and Grant 84336650, in part by the National Council for Scientific and Technological Development (CNPq) under Grant 304192/2016-3, in part by the Petrobras under Grant 2017/00702-6, in part by the National Funds (OE), through Fundação para a Ciência e a Tecnologia, (FCT) I.P., in the scope of the Framework Contract foreseen in the numbers 4, 5 and 6 of the article 23, of the Decree-Law 57/2016, of August 29, changed by Law 57/2017, of July 19. The work of Carlos Marques was supported by the FCT through the program under Grant UID/CTM/50025/2019, in part by the National Funds through the Fundação para a Ciência e a Tecnologia / Ministério da Educação e Ciência, and in part by the European Regional Development Fund under the PT2020 Partnership Agreement.

ABSTRACT We report the development of an optimization approach for diaphragm-embedded optical fiber sensors, which was applied on the pressure, force and liquid level assessment using chirped fiber Bragg gratings (CFBGs) inscribed in cyclic transparent optical polymer (CYTOP) fibers. The inscription was performed using the plane-by-plane method with a femtosecond laser, whereas the diaphragm optimization was performed through the multi-objective particle swarm optimization (MOPSO). The objective functions for the optimization were obtained from numerical simulation using the finite element method of diaphragms with different thickness and diameters. The MOPSO resulted in a set of solutions with thickness and diameter aiming the optimization of sensitivity and linearity of diaphragm-embedded CFBG sensors. Three configurations were chosen with different values sensitivity and linearity. Experimental analysis was performed in each configuration for temperature and pressure variations, where the results confirmed the different sensitivity and linearity levels for each chosen configuration. Two applications were analyzed for the proposed configurations with higher sensitivity and linearity: one for force estimation over a 200-N range and the other for sub-millimeter assessment of liquid level over a 50-cm range. In order to obtain a highly reliable and accurate system, a novel data integration method for chirped FBGs was proposed. In this case, the estimation of force, pressure or liquid level was performed considering the contributions of both wavelength shift and full width half maximum (FWHM) variations. The proposed approach resulted in error improvement of 60% for all cases and for all parameters analyzed.

INDEX TERMS Chirped fiber Bragg gratings, polymer optical fibers, optimization, pressure sensors.

I. INTRODUCTION

In recent years, optical fiber sensors have experienced a growth and widespread use due to advantages such as compactness, lightweight configuration, chemical stability, multiplexing capabilities and immunity to electromagnetic interferences and passive operation [1]. Furthermore, there is no electric signals in the sensor head, which makes optical fiber sensors an intrinsic safe solution for harsh and explosive environments [2]. For these reasons, optical fiber sensors have been widely used in medicine [3], healthcare [4], industrial applications [5], structural health monitoring [6] and in radioactive environments [7].

Among many optical fiber-based sensing approaches, e.g. nonlinear effects [8], intensity variations [9], interferometers [10] and reflectometry [11], fiber Bragg gratings (FBGs) are popularly employed to the measurement of diverse industrial and structural parameters, such as strain,

The associate editor coordinating the review of this manuscript and approving it for publication was Sanket Goel.

This work is licensed under a Creative Commons Attribution 4.0 License. For more information, see http://creativecommons.org/licenses/by/4.0/

pressure, liquid level, temperature, humidity and even detection of specific chemical compounds [12]. The reason for such widespread use is its high resolution, sensitivity and reliability of such sensing scheme, which is mainly related to their wavelength-encoded data that can be also be used to provide multiplexing capabilities (i.e., the possibility of inscribing dozens of sensors in the same fiber) [13]. Such advantages resulted in a compact and simple sensing solution for multipoint and multiparameter measurements in a quasi-distributed configuration [14].

FBGs are created through a refractive index modulation when the fiber is exposed to a periodic intensity pattern [13]. If the period is constant, a uniform FBG is created, whereas a non-constant period is used, it results in a non-uniform FBG, which can be classified as phase-shift or chirped FBG depending on the period variation [15]. Chirped FBGs are created through a linear variation of the period on the refractive index modulation [16]. Thus, there is a variation on the Bragg wavelength along the grating region, which can be regarded as uniform FBGs in a cascaded configuration, resulting in a broader backscattered spectrum, where the full width half maximum (FWHM) can be as high as tens of nanometers [17]. Besides their use as dispersion compensator in communication systems, the spectral dependence with strain or temperature profiles along the grating length make chirped FBGs suitable for diverse applications such as thermal profiling applications [18], strain distribution [16], and impact detection [17]. In addition, it is possible to analyze both the wavelength shift and FWHM variation in order to obtain simultaneous measurements and temperature insensitive systems [19].

Advances on polymer processing, characterization and photosensitivity analysis have resulted in the development of FBGs in polymer optical fibers (POFs) [20]. Such fibers have intrinsic advantages over the conventional silica optical fibers for sensors applications due to their higher strain limits, fracture toughness, lower Young's modulus and flexibility [21]. These advantages result to sensors with higher sensitivity and dynamic range for mechanical parameters measurement [22]. As the main drawback of most POFs are their high attenuation at 1550 nm wavelength region, perfluorinated POFs, such as CYTOP, have been proposed as a viable alternative for optical signals transmission at 1550 nm [23]. However, their ultraviolet (UV) resistance prevents efficient FBG inscription using conventional UV lasers. For this reason, a plane-by-plane direct inscription method was proposed in [24] for a single peak FBG spectrum in multimode CYTOP fibers using a femtosecond (fs) laser operating at 517 nm, which enabled the inscription of long arrays in this fiber [25], [26] as well as Fabry-Perot cavities and chirped FBGs[27].

Since the FBGs are intrinsically sensitive to strain, temperature and, for some polymers fibers to humidity variations as well. The use of these sensors in monitoring another mechanical parameter occurs by embedding the FBGs in different structures. Diaphragms are one of the most commonly employed structures for FBG embedment. They are used on the assessment of vibration [28], acceleration [29], plantar pressure [30], force [31] and liquid level [32]. For such different parameters, with different requirements of sensitivity and dynamic range, the diaphragm design is of critical importance, since the dynamic response of the sensor is dependent on the diaphragm geometry [33] and material behavior [34]. These conflicting parameters generally result in a multi objective optimization problem, where it is desirable to have maximum sensitivity, linearity or dynamic range for the sensor system.

This paper focus on the optimal design of 3-D printed diaphragms, with embedded chirped FBGs on CYTOP fibers, so that pressure sensors can be fabricated in practice with both maximum sensitivity and linearity. No exact optimization formulation is viable in this case, so optimization heuristics that have been proposed throughout the years, such as genetic algorithms and particle swarm optimization (PSO) algorithms [35], can be used to perform educated search over candidate solutions across a given population [36]. Herein diaphragms were optimized through the multi objective PSO (MOPSO) for simultaneously maximum linearity and sensitivity over a population of chirped FBGs in CYTOP fibers embedded in 3D-printed circular diaphragms different diameter and thickness. Such constructive parameters have intricate relationships with sensor linearity and sensitivity, thus only numerical simulations (using, for example, the finite element method) can accurately represent the strain distribution over the diaphragms, and more importantly, strain transfer to the FBG. On the other hand, it is prohibitively time consuming the task of generating large populations of numerically simulated diaphragms. Then, this paper proposes a simplified method which is used to construct three different configurations of diaphragms obtained from the MOPSO. They were 3D-printed and a chirped FBG inscribed in CYTOP fiber was embedded in each diaphragm for the assessment of pressure and liquid level, which was obtained by analyzing both the wavelength and FWHM of the grating spectra.

The contributions of this work are twofold: (i) the development of guidelines for diaphragm design, which can be used not only on chirped FBG sensors, but also on any optical fiber sensor based on diaphragms. (ii) To the authors' knowledge, this is the first application of chirped FBGs in CYTOP fibers, where it is possible to obtain a temperature-insensitive system that is also capable of measuring pressure with higher accuracy through the data integration between the wavelength shift and FWHM.

II. DIAPHRAGM DESIGN AND OPTIMIZATION

The diaphragm design was performed considering the material and geometric parameters; thickness and diameter. Since the diaphragm is fabricated through 3D printing in a flexible material, the thermoplastic polyurethane (TPU) was the material considered in the numerical analysis. For the analysis, we consider a Young's modulus of 0.25 GPa, Poisson's ratio of 0.49 and density of 1190 kg/m^3, where the

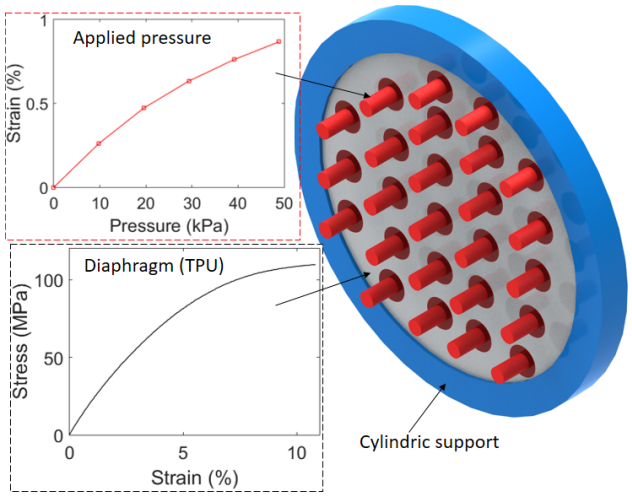

FIGURE 1. A schematic representation of the diaphragm loading configuration used in the FEM simulation. Figure insets show the stress-strain curve of the TPU and the strain at the diaphragm center for different pressures.

stress-strain curve obtained on the TPU characterization in an universal tensile testing machine (shown in Fig. 1 inset) was also included in the numerical simulation.

The numerical simulation was performed using the finite element method (FEM), where the inputs for the model are a fixed cylindrical support and constant pressures applied on the diaphragm front face (see Fig. 1). In this case, the strain at the diaphragm center is analyzed as a function of the applied transverse pressure. In the simulations, the applied pressures varied from 0 to 48.9 kPa. The strain in the diaphragm center was analyzed as a function of the applied pressures and the slope and the correlation with a linear response were analyzed in order to estimate the sensitivity and linearity of the diaphragm strain response. Figure 1 shows a schematic representation of the configuration used for the numerical analysis, the TPU stress-strain curve and the strain response (as a function of the applied pressure) for the diaphragm with 1 mm thickness and 50 mm diameter. It is possible to observe in the strain response shown in Fig. 1 the sensitivity and linearity of this specific diaphragm configuration.

These numerical simulations are repeated for diaphragms with different diameter and thickness, where the thickness analyzed ranged from 0.25 mm to 1.50 mm and the diameter from 10 mm to 50 mm. The upper and lower bounds for the diaphragm geometric parameters were defined considering the limitations on the diaphragm fabrication, which include the spatial resolution of the 3D printer as well as the limits of the experimental prototype for the transverse pressure (or hydrostatic pressure) sensing.

The sensitivity and linearity of the strain response were estimated for each diaphragm's configuration and a correlation between the performance parameters, i.e., sensitivity and linearity with respect to the diaphragm thickness and diameter was obtained. Thus, a polynomial regression was performed to correlate the diaphragm geometric parameters

TABLE 1. Parameters employed on the sensor responses estimation.

Parameter	Value	Parameter	Value
s_1	0.136	l_3	-8.6×10^{-3}
s_2	2×10^9	l_4	1.3×10^{-3}
l_1	0.95	l_5	1.27×10^{-5}
l_2	0.22	a	-4.5×10^{-3}

(thickness and diameter) with the sensitivity and linearity, resulting in two equations. Such equations are applied as the objective functions for the proposed MOPSO algorithm. The objectives are the maximization of sensitivity and linearity through the choice of the correct diaphragm thickness and diameter.

Particle Swarm Optimization (PSO) is one of the most popular meta-heuristics, inspired in the flight of bird flocks and proposed by Kennedy and Eberhart [35]. In this problem, a Multi-Objective PSO is used and a set of optimal solutions, called the Pareto front, are provided. The Pareto front is based in the concept of dominance in order to indicate and compare the quality degree of different solutions, i.e., solution x_1 dominates x_2 if and only if, for all purposes involved in the domain of the function, x_1 is not worse than x_2 in any order and there is at least one goal in which x_1 is better than x_2. The proposed problem formulation can be expressed as follows [36]:

$$linearity = l_1 + l_2 \times e^a \times D + l_3 \times e^2, \\ +1.3 \times 10^{-3} \times e \times D + 1.27 \times 10^{-5} \times D^2 \quad (1)$$

$$sensitivity = \frac{s_1 \times D^2}{2 \times 10^9 \times e^2}, \quad (2)$$

where $0.2\ mm \leq\ e\ \leq 1.5\ mm$ and $10\ mm \leq\ D\ \leq 50\ mm$. These limits were chosen due to resolution restrictions of the 3D printer (0.05 mm) and the limits on the experimental prototype for the sensor characterizations. In addition, the parameters of the regressions in Eqs. (1) and (2) are presented in Table 1.

The goal of MOPSO is to get the Pareto front among the possible solutions x_i = [thicknessi, Diameteri]. Since it is a meta-heuristic, inspired by the flight of bird flocks, the operating principle is based on the experience of each bird and the overall swarm experience to look for the optimal Pareto curve at each iteration. These Pareto front solutions are stored in a repository. The birds have their position altered based on a weighting between their previous speeds, their current distance from their best experience, and their current distance from their best group experience. Mathematically, the creation of the swarm, the speed update and the position of the birds are determined with the following equations [36]:

$$x_i = x_{\min} + rand(0, 1) \times (x_{\max} - x_{\min}), \quad (3)$$

$$\upsilon_i(t) = \omega \times \upsilon_i(it - 1) + c_1 \times (p_i - x_i(it - 1), \\ +c_2 \times (g - x_i(it - 1)) \quad (4)$$

$$x_i(t) = x_i(it - 1) + \upsilon_i(t), \quad (5)$$

where x_i is the i_{th} swarm component (one of the solutions analyzed), x_{max} is maximum value of component xi, whereas

its minimum value is x_{min}. In addition, rand (0,1) is a random number between 0 and 1, v_i (it) is the speed of swarm component i in the iteration it, and w is an inertial factor. c_1 and c_2 are the acceleration factors 1 and 2, respectively. The best result obtained by a component i is the parameter p_i, whereas the best result obtained by the swarm in the Pareto front repository is g.

The iterative process of this meta-heuristic search can be summarized following 6 steps: (i) initialize the solution vector using equation 1; (ii) evaluate the solutions using the dominance concept; (iii) update the best individual result by bird (p_i) using the dominance concept. Step (iv) update the Pareto front repository and randomly choose g from the Pareto front solutions; (v) update the solution vector using equations 2 and 3; Finally, step (vi) consists in returning to step 2, repeating the procedure until the stopping criterion is met.

Figure 2 shows the results obtained in the optimization using MOPSO. The x-axis presents the sensitivity, whereas the y-axis shows the linearity for different diaphragm configurations. In Fig. 2 insets, the strain distribution on the different configurations is presented for a pressure of 9 kPa. These configurations were the ones chosen on the diaphragm fabrication. As there are a tradeoff between the sensitivity and linearity, the chosen solutions represent the ones with highest sensitivity, linearity and another solution that represents a medium sensitivity and linearity.

Regarding Fig. 2, three configurations were chosen for the diaphragm fabrication. Configuration 1 with diaphragm thickness of 0.8 mm and diameter of 30 mm, which is the configuration with highest linearity and lowest sensitivity among the ones tested. Configuration 2: diameter of 45 mm and 1.2 mm thickness, which provides a combination of medium sensitivity and linearity. Finally, Configuration 3 (with 0.2-mm thickness and 42-mm diameter) results in the highest sensitivity, but with the lowest linearity between the chosen configurations. It is also worth noting that we choose the configurations based on the 3D printer resolution (0.05 mm). For this reason, there some configurations were not chosen, since they resulted in a diaphragm thickness and/or diameter that the 3D printer was not able to fabricate, e.g., the configuration indicated in Fig. 2 (with a dashed blue circle), where the diaphragm has a thickness of 0.42 mm, which is below the 3D printer resolution on z-axis of the printer, since the printer, with the 0.05 mm resolution at this axis, will only be able of producing the thickness of 0.4 mm or 0.45 mm and not 0.42 mm.

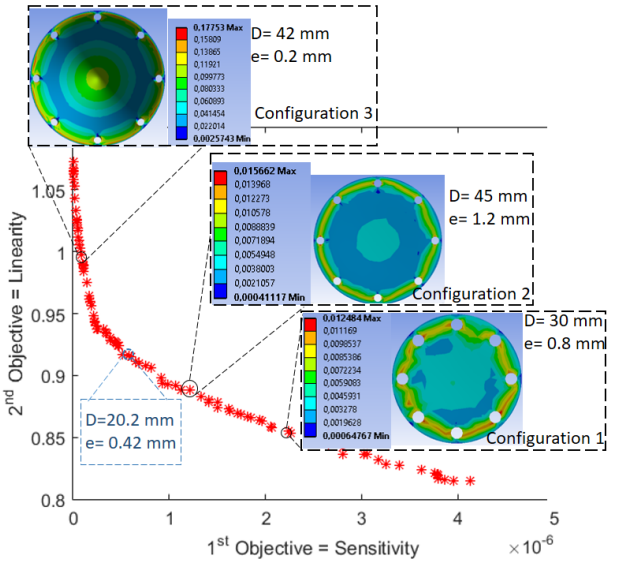

FIGURE 2. Results obtained in the MOPSO with linearity and sensitivity as the objective functions. The figure insets show the strain distribution for each configuration considering a pressure of 9 kPa.

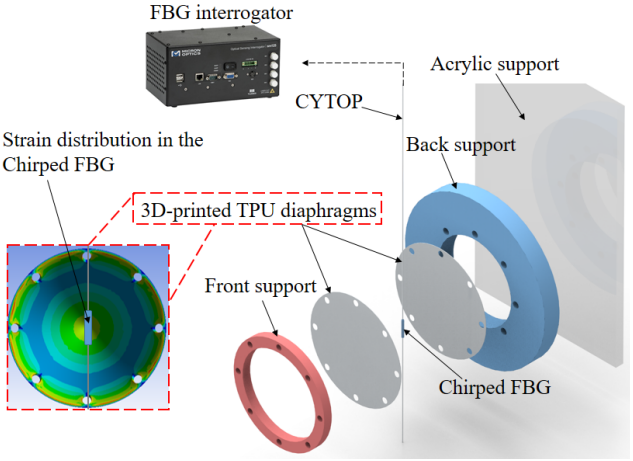

FIGURE 3. A schematic representation of the sensor assembly and connection. The figure inset shows the strain distribution in the diaphragm, which is transmitted to the chirped FBG.

III. EXPERIMENTAL ANALYSIS

A. EXPERIMENTAL SETUP

The diaphragms (for all three configurations) were fabricated using the TPU material in the 3D printer Sethi3D S3 (Sethi, Brazil), where 100% infill density and 0.02 mm of layer thickness. The diaphragms had the design shown in Fig. 3 for their positioning on the experimental setup, which was comprised of two supports, for the front and back faces of the diaphragm. The supports were also fabricated through 3D printing in a poly-lactic acid (PLA) material, where the infill density was also 100%. The supports and the diaphragm were connected to an acrylic support through a bolt connection.

The reflected spectra of the chirped FBGs were acquired with the FBG interrogator sm125 (Micron Optics, USA) having a 1-pm spectral resolution. The chirped FBGs were inscribed in CYTOP fibers (Chromis Fiberoptics Inc.) using the plane-by-plane direct write method using a fs laser operating at 517 nm with 220-fs pulse duration (HighQ laser femtoREGEN). The fibers with 120-μm core diameter, 20-μm cladding thickness and polycarbonate overcladding were positioned on an air-bearing stage with nanometer resolution capable of positioning the fiber with respect to the

laser focus (focused through a ×50 objective lens). In order to provide the chirp in the grating period, each plane had a 7.65 pm increase resulting in a difference between the first and final period (2000 periods with a total of about 5 mm), resulting in a chirp of 2.2 nm/mm [27].

As presented in Fig. 3 inset, there was a strain distribution on the diaphragm in the region where the chirped FBG was positioned. Thus, there was a strain distribution on the grating region due to the strain transmission from the diaphragm to the POF, which resulted not only in the wavelength shift, but also in the FWHM, as depicted in [16], whereas, the uniform distribution of the temperature on the diaphragm led to only a wavelength shift.

For the pressure characterization, calibrated weights are positioned on the support shown in Fig. 3, which has a known area. In this case, the pressure range is from 0 kPa to 18.5 kPa in steps of ∼ 3.7 kPa. Moreover, a temperature characterization was performed, where the sensors were positioned inside the climate chamber 1/400 ND (Ethik Technology, Brazil) with a temperature variation from 30°C to 60°C, in steps of 10°C. In addition, the dependency of the FWHM with the temperature variations on the proposed sensor system were investigated, since such variations can be related to the diaphragm parameters due to the thermal expansion of the TPU material.

B. DIAPHRAGM-EMBEDDED CYTOP CHIRPED FBG SENSOR CHARACTERIZATIONS AND DATA INTEGRATION

The configurations (Fig. 2) were tested in the aforementioned experimental setup. The diaphragm parameters and chirped POFBG embedment lead to different initial strain distributions on the grating region, which can influence the initial chirped FBG spectrum for each configuration. In order to verify this dependency, Fig. 4 presents the reflected spectrum of the chirped FBG inscribed in CYTOP fibers for each configuration.

The results presented in Fig. 4 indicate that the diaphragm configuration, thickness and diameter in this case, can influence the spectrum of the FBG when it is embedded in the diaphragm structure. However, such variations depend not only on the diaphragm parameters but also on the embedment method, as shown in [36], where the same diaphragm can have different responses by changing the diaphragm assembly due to different bolt pre-tension. Such dependency on the assembly explains the lower central wavelength and FWHM of Configuration 2, when compared with the other configurations. It also should be noted that such lower central wavelength of Configuration 2 is also related to its higher diameter and thickness (see Fig. 2), which lead to lower strain distribution on the POF when it is embedded within the diaphragm. This also results in a lower FWHM as depicted in Fig. 4(d). In contrast, Configuration 3 has the lowest thickness, which can lead to higher strain transmission from the diaphragm to the CYTOP, resulting in the highest central wavelength. On the other hand, Configuration 1, with its lowest diameter can result in a higher strain distribution in

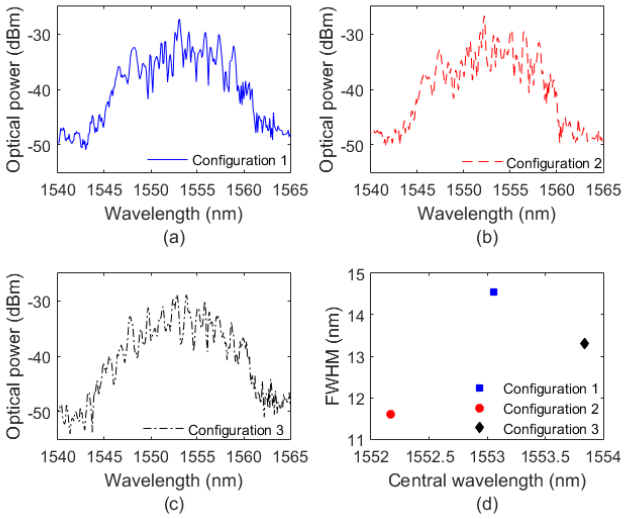

FIGURE 4. Reflected spectra of the chirped POFBG embedded in the diaphragms with different configurations. (a) Configuration 1, (b) Configuration 2 and (c) Configuration 3. (d) Central wavelength and FWHM for the chirped POFBG at different configurations.

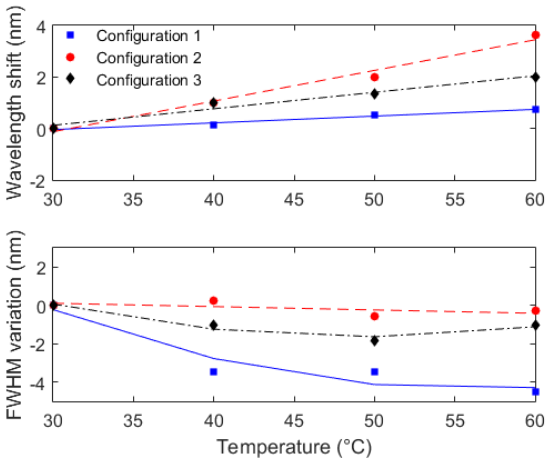

FIGURE 5. Wavelength shift and FWHM variation as a function of the temperature for each sensor configuration.

the grating region during the chirped FBG embedment, which leads to a higher FWHM.

It is important to emphasize that the results in Fig. 4 are related to the embedment method of the POF sensors in the diaphragm structures. The conclusions regarding initial central wavelength and FWHM are not related to the sensitivity and/or linearity of these parameters with pressure or temperature. In order to verify the behavior of the chirped FBG spectral response as a function of the temperature, Fig. 5 shows the results obtained in temperature characterizations for each configuration.

Although the optimization process proposed only considered the effects of pressure on the diaphragm response, the results presented in Fig. 5 indicate that the temperature also plays an important role on the sensor response. Thus, in applications where there are temperature variations, the thermal response of the diaphragm should also be

considered regarding the selection of thickness and diameter. As the temperature increases, there is also an increase of the thermal-induced strain on the diaphragm, which can be transmitted to the chirped FBG. This effect can explain the higher wavelength shift in Configuration 2, where there is the highest thickness on the diaphragm.

In addition, such high thickness can also be related to the lower FWHM variation due to uniform distribution of the thermal-induced strain on the diaphragm, resulting in uniform strain transmission to the grating region, which leads to a lower variation of the FWHM. If a temperature sensor with chirped FBGs is considered, Configuration 2 presents the highest sensitivity and linearity, whereas Configuration 3 presents the lowest wavelength shift, but with a higher FWHM variation. Due to its temperature dependency, the pressure and application tests are performed at constant (room) temperature.

Thereafter, the pressure characterization is performed with the proposed sensors, where the results obtained in such experimental analysis (Fig. 6). In this case, regarding to the wavelength shift, the sensor behavior is similar to the predicted simulations, where the lowest sensitivity and highest linearity (among the ones tested) were obtained for Configuration 3, whereas the highest sensitivity and lowest linearity were found in Configuration 1. As predicted in the MOPSO, Configuration 2 offers higher linearity than Configuration 1 and higher sensitivity when compared with Configuration 3. If the FWHM variation is analyzed, both Configurations 2 and 3 presented similar response, whereas Configuration 1 presented the lowest FWHM variation. The reason for this behavior is related to the diaphragm's diameter of each configuration, where Configuration 1 (with the smallest diameter among the ones tested) presented the lowest FWHM variation, whereas Configurations 2 and 3, with similar diameter (Fig. 2) also presented similar FWHM variation, which indicates the dependency of the diaphragm diameter with the FWHM; a larger diameter can be related to a higher non-uniformity on the diaphragm strain distribution (transmitted to the chirped FBG). The strain variation on the diaphragm is presented in the insets of Fig. 2, where it is possible to observe that the distribution with higher uniformity is the one obtained in the simulations of Configuration 1, which also presented the lowest FWHM variation.

Figure 6 indicates that the pressure applied on the diaphragm leads both the wavelength shift and the FWHM variation in all analyzed cases. Therefore, if the whole spectral response is analyzed, there are two parameters to be correlated with the pressure variation. For this reason, it is possible to perform a polynomial regression through the least squares method for estimating the applied pressure from both the wavelength shift and FWHM variation of each proposed sensor's configurations. Considering the results obtained in the sensor's characterization, the polynomial regressions using the FWHM variation were performed considering the behavior of the wavelength shift, i.e., a polynomial degree 1 for Configurations 1 and 2, degree 2 for Configuration 3.

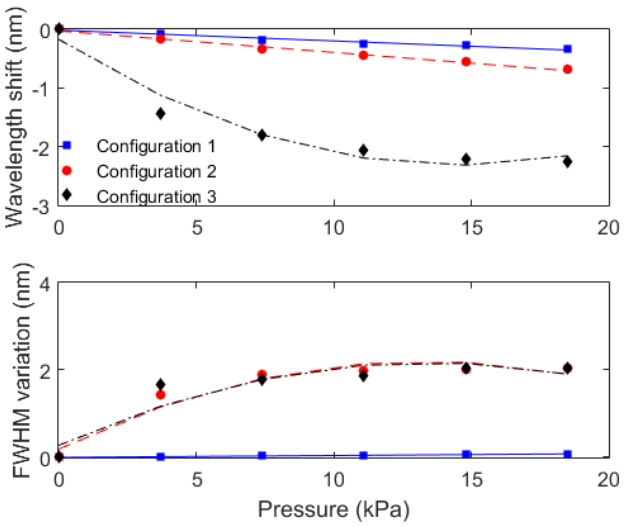

FIGURE 6. Wavelength shift and FWHM variation as a function of the pressure variation for each sensor configuration.

Such polynomial regressions resulted in Eq. (6) - (8) for Configurations 1, 2, and 3, respectively, where the applied pressure is estimated from the FWHM variation (ΔB) and wavelength shift ($\Delta\lambda$).

$$p_{c1} = 0.2881 + 17.68\Delta\lambda + 155.2\Delta B, \quad (6)$$

$$p_{c2} = 0.07117 + 30.61\Delta\lambda + 1.311\Delta B, \quad (7)$$

$$p_{c3} = 0.003938 + 37.63\Delta\lambda + 25.37\Delta B + 18.16\Delta\lambda^2, + 9.16\Delta B\Delta\lambda \quad (8)$$

where p_{c1}, p_{c2} and p_{c3} are the estimated pressures using Configurations 1, 2 and 3, respectively.

The estimated pressure using each configuration and its comparison with the applied pressure is presented in Fig. 7, where the root mean squared errors (RMSEs) between the estimated and applied pressures are showed for each configuration.

As presented in Fig. 7, Configuration 2 has the lowest RMSE, and all tested configurations have a RMSE below 1 kPa, which can be regarded as low pressure errors considering the whole range of the pressure characterization. If the results of the pressure estimation (Fig. 7) are compared with the FWHM variation and wavelength shift as a function of the pressure (Fig. 6), the lower errors obtained with Configuration 2 are related to the lower difference between the polynomial regressions and the measured responses for FWHM variation and wavelength shift.

Nevertheless, if a larger measurement range is necessary, the Configuration 1 is the most suitable one, since both FWHM and wavelength shift presented a linear response as function of the applied pressure. Thus, one can expect that if the pressure variation exceeds 18 kPa, Configuration 1 will be able to track and estimate these differences, whereas Configurations 2 and 3 will present errors or inaccuracies in the pressure estimation, since their FWHM variations present a saturation tendency in pressures higher than 10 kPa.

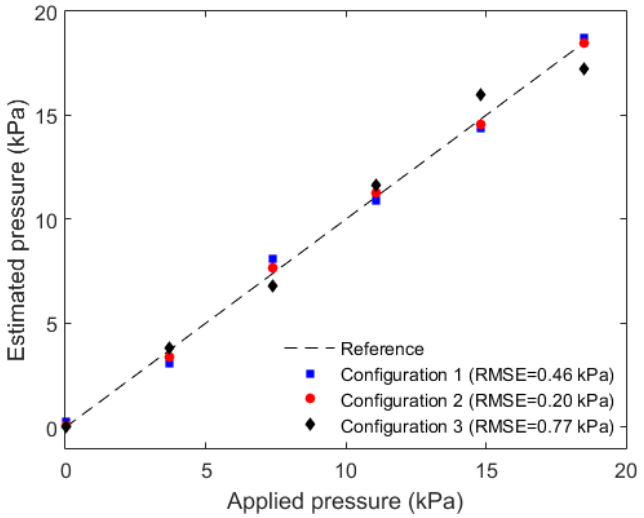

FIGURE 7. Pressure estimation using the data integration approach for all tested configurations.

For Configuration 3, even the wavelength shift presents such behavior, where the sensor is not linear for pressures exceeding 5 kPa. On the other hand, the highest signal variation occurs in Configuration 3, which can be regarded as the configuration with the highest sensitivity and resolution. If the FBG interrogator with 1-pm resolution is considered, configuration 3 is capable of measuring applied pressures as low as 4.11 Pa. The behaviors of the proposed configurations lie within the MOPSO predictions, where Configuration 1 has the highest linearity and Configuration 3 the highest sensitivity.

IV. APPLICATIONS OF THE PROPOSED DESIGNS

Considering the analysis presented in Section II and III, two different applications were proposed. In the first application, the diaphragm-embedded chirped FBG was used for force assessment applications, where forces as high as 200 N were applied on the system in steps of 50 N. In the second application, the proposed sensor system was used on the liquid level assessment through the hydrostatic pressure variation. In this case, it was desirable that the sensor had high resolution in order to measure the level with sub-millimeter resolution in a 50-cm range.

Configuration 1 was used for the force assessment application, providing the highest linearity when both FWHM variation and wavelength shift are analyzed. Figure 8(a) shows the experimental setup for force application, whereas Fig. 8(b), (c) and (d) present the wavelength shift, FWHM variation and force estimation using the chirped FBG in Configuration 1. The results presented in Fig. 8 show that the sensor in Configuration 1 maintains its linear behavior even in a larger deflection range than the ones tested on the pressure characterizations. Such features make Configuration 1 suitable for applications that require large dynamic range from the sensor system, which include ground reaction forces assessment in movement analysis, force assessment in axial bearings and axles of mechanical system, as well as force estimation in end effectors of robotic manipulators.

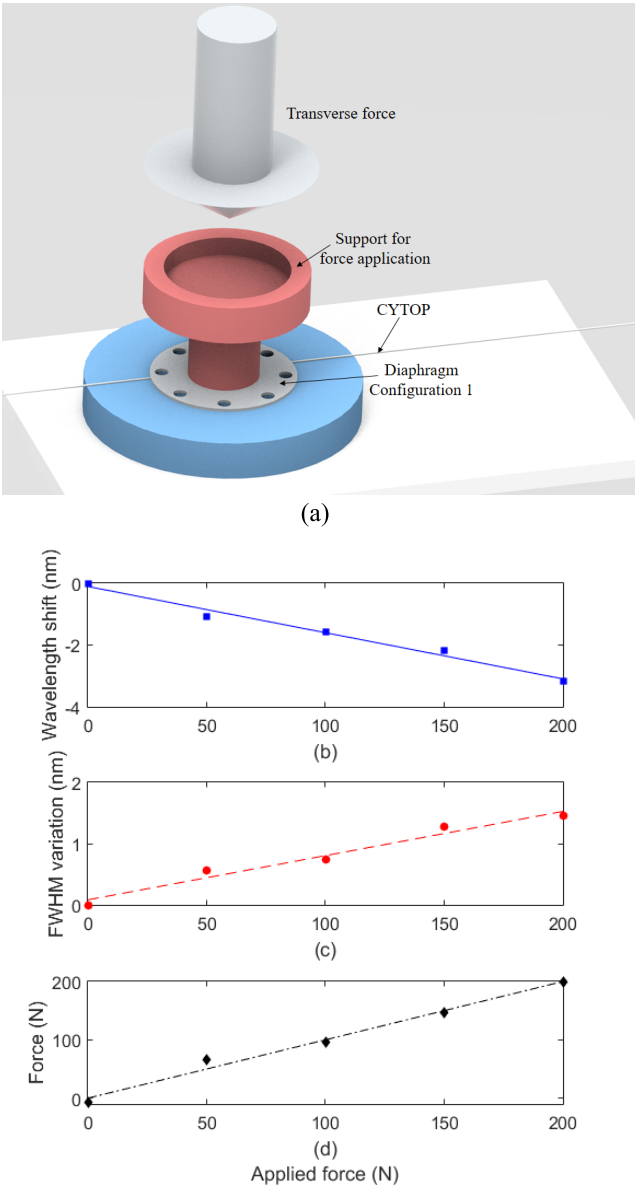

FIGURE 8. (a) Experimental setup, (b) Wavelength shift, (c) FWHM variation and (d) force estimation for Configuration 1.

Regarding to the errors on the force estimation, the proposed approach in which both FWHM and wavelength shift are used on the polynomial regression for force estimation resulted in a RMSE of about 7.9 N, whereas the rate of variation on the spectral response resulted in a force resolution of 0.06 N (considering the 1-pm resolution of the FBG interrogator). In the conventional approach for parameter estimation using FBGs, only the wavelength shift or the FWHM are used on the sensor's response estimation. In these cases, the RMSEs are 9.3 N for the estimation using only the wavelength shift and 12.7 N for the case when only the FWHM is analyzed. Thus, the proposed data integration approach, where FWHM and wavelength are combined in order to provide a better estimation of the measurand (force in this case) results in a 37 % reduction of the measurement errors.

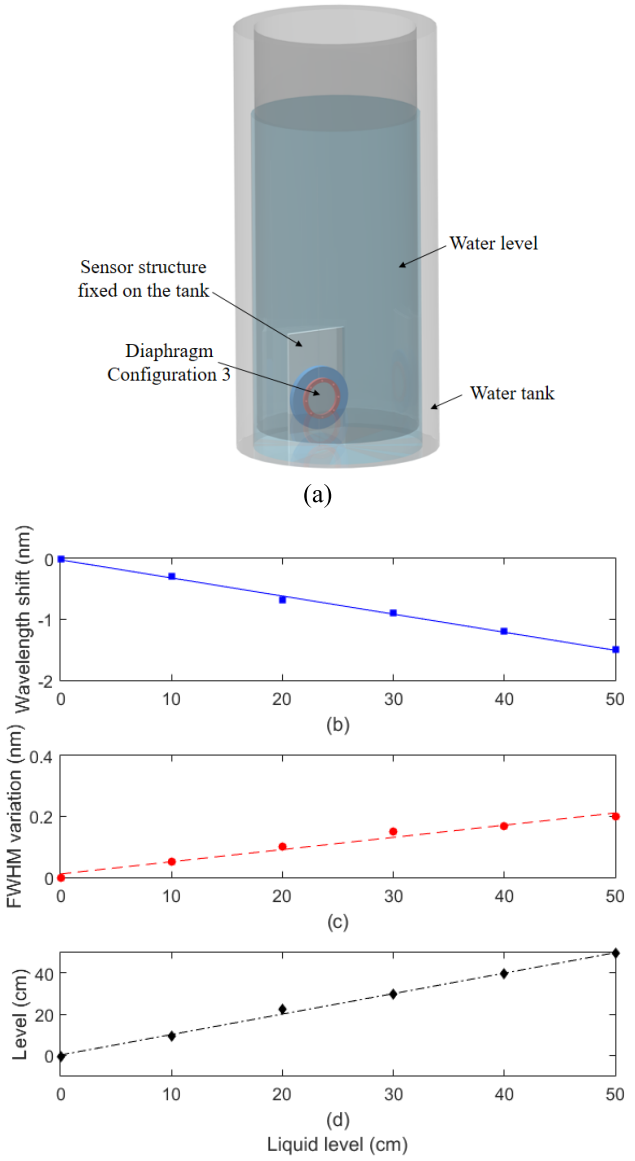

FIGURE 9. (a) Experimental setup, (b) Wavelength shift, (c) FWHM variation and (d) liquid level estimation for Configuration 3.

The second proposed approach is the liquid level assessment, where the requirements are high resolution in a limited operation range. Considering the results obtained in Section II and III, Configuration 3 is most suitable for this application. The chirped FBG with the diaphragm in Configuration 3 is positioned on the experimental setup shown in Fig. 10(a), where there is a maximum liquid level variation of 50 cm, which was performed in steps of 10 cm. The wavelength shift, FWHM variation and liquid level estimation are presented in Fig. 10(b), (c) and (d), respectively.

The results obtained in Fig. 10(d) shows the feasibility and high accuracy of the proposed data integration approach, where a RMSE lower than 1 cm was obtained when wavelength shift and FWHM variation were used on the liquid level estimation, whereas the error using only one spectral information was as high as 2.5 cm. In addition, if the error is further reduced, the proposed sensor configuration can achieve sensing resolution of 0.3 mm (when the FBG interrogator with 1-pm resolution is considered).

V. CONCLUSION

This paper presented the development and application of a chirped FBG inscribed in CYTOP fibers, combined with an optimization method for diaphragm-embedded optical fiber sensors. The strain distribution on the diaphragms were analyzed through the FEM, where the linearity and strain variation of the strain at the diaphragm center as function of the diaphragm thickness and diameter were used as the objective functions for MOPSO algorithm. Thereafter, 3 diaphragm configurations were chosen based on the Pareto front obtained on the MOPSO, one with higher sensitivity and lower linearity (Configuration 3), one with lower sensitivity and higher linearity (Configuration 1) and one with a balance between sensitivity and linearity (Configuration 2).

The chirped POFBGs were embedded in each diaphragm and the pressure response of those systems were analyzed as function of the wavelength shift and FWHM variation. The results obtained in the characterizations confirmed the predictions from the numerical and optimization models. For this reason, two applications were proposed: one for large force assessment and the other for liquid level measurement. The first application demands a sensor with high linearity, resulting in a larger dynamic range. For this reason, the Configuration 1 was used, whereas the liquid level application needs a sensor with high sensitivity, leading to higher sensing resolution, which is obtained with Configuration 3.

In addition, we also proposed novel data integration for chirped FBGs, where both wavelength shift and FWHM variations were used on the pressure, force or liquid level estimation. Compared with the conventional approach using only the wavelength shift or FWHM, the proposed data integration resulted in an error reduction of 37% and 60% for Configurations 1 and 3, respectively. Therefore, the proposed approach for data integration is a feasible method for obtained chirped FBG sensors with higher accuracy.

Furthermore, the proposed optimization approach provides guidelines for the diaphragm design considering different applications for any diaphragm-embedded optical fiber sensor. Finally, to the authors' best knowledge, this the first application of chirped FBGs inscribed in CYTOP fibers, which presents intrinsic advantages over conventional silica fibers due to its potentially higher sensitivity and dynamic range. However, the pressure characterizations were performed in constant temperature conditions and the temperature characterization shows a dependency on the sensitivity and linearity for temperature measurements on the diaphragm thickness and diameter. This dependency as well as the viscoelastic effects and temperature cross-sensitivity in diaphragms with different configurations will be further explored in future works.

REFERENCES

[1] K. T. V. Grattan and T. Sun, "Fiber optic sensor technology: An overview," *Sens. Actuators A, Phys.*, vol. 82, no. 1, pp. 40–61, 2000.

[2] A. Cusano, A. Cutolo, and J. Albert, *Fiber Bragg Grating Sensors: Market Overview and New Perspectives*. Potomac, MD, USA: Bentham Science Publishers, 2009.

[3] V. Mishra, N. Singh, U. Tiwari, and P. Kapur, "Fiber grating sensors in medicine: Current and emerging applications," *Sens. Actuators A, Phys.*, vol. 167, no. 2, pp. 279–290, Jun. 2011.

[4] A. G. Leal-Junior, C. A. R. Diaz, L. M. Avellar, M. J. Pontes, C. Marques, and A. Frizera, "Polymer optical fiber sensors in healthcare applications: A comprehensive review," *Sensors*, vol. 19, no. 14, p. 3156, Jul. 2019.

[5] C. A. R. Diaz, A. Leal-Junior, C. Marques, A. Frizera, M. J. Pontes, P. F. C. Antunes, P. S. B. Andre, and M. R. N. Ribeiro, "Optical fiber sensing for sub-millimeter liquid-level monitoring: A review," *IEEE Sensors J.*, vol. 19, no. 17, pp. 7179–7191, Sep. 2019.

[6] D. Kinet, P. Mégret, K. Goossen, L. Qiu, D. Heider, and C. Caucheteur, "Fiber Bragg grating sensors toward structural health monitoring in composite materials: Challenges and solutions," *Sensors*, vol. 14, no. 4, pp. 7394–7419, Apr. 2014.

[7] C. Broadway, D. Kinet, A. Theodosiou, K. Kalli, A. Gusarov, C. Caucheteur, and P. Mégret, "CYTOP fibre Bragg grating sensors for harsh radiation environments," *Sensors*, vol. 19, no. 13, p. 2853, Jun. 2019.

[8] Y. Mizuno, N. Hayashi, H. Fukuda, K. Y. Song, and K. Nakamura, "Ultrahigh-speed distributed Brillouin reflectometry," *Light Sci. Appl.*, vol. 5, no. 12, p. e16184, Dec. 2016.

[9] A. G. Leal-Junior, A. Frizera, L. Vargas-Valencia, W. M. Dos Santos, A. P. L. Bo, A. A. G. Siqueira, and M. J. Pontes, "Polymer optical fiber sensors in wearable devices: Toward novel instrumentation approaches for gait assistance devices," *IEEE Sensors J.*, vol. 18, no. 17, pp. 7085–7092, Sep. 2018.

[10] R. Oliveira, L. Bilro, and R. Nogueira, "Fabry-Pérot cavities based on photopolymerizable resins for sensing applications," *Opt. Mater. Express*, vol. 8, no. 8, p. 2208, Aug. 2018.

[11] M. P. Hiscocks, M. A. Van Eijkelenborg, A. Argyros, and M. C. J. Large, "Stable imprinting of long-period gratings in microstructured polymer optical fibre," *Opt. Express*, vol. 14, no. 11, p. 4644, 2006.

[12] C. Broadway, R. Min, A. G. Leal-Junior, C. Marques, and C. Caucheteur, "Toward commercial polymer fiber Bragg grating sensors: Review and applications," *J. Lightw. Technol.*, vol. 37, no. 11, pp. 2605–2615, Jun. 1, 2019.

[13] K. O. Hill and G. Meltz, "Fiber Bragg grating technology fundamentals and overview," *J. Lightw. Technol.*, vol. 15, no. 8, pp. 1263–1276, Aug. 1997.

[14] A. G. Leal-Junior, A. Frizera, A. Theodosiou, C. Diaz, M. Jimenez, R. Min, M. J. Pontes, K. Kalli, and C. Marques, "Plane-by-plane written, low-loss polymer optical fiber Bragg grating arrays for multiparameter sensing in a smart walker," *IEEE Sensors J.*, vol. 19, no. 20, pp. 9221–9228, Oct. 2019.

[15] C. Marques, A. Leal-Junior, R. Min, M. Domingues, C. Leitão, P. Antunes, B. Ortega, and P. André, "Advances on polymer optical fiber gratings using a KrF pulsed laser system operating at 248 nm," *Fibers*, vol. 6, no. 1, p. 13, Mar. 2018.

[16] D. Tosi, "Review of chirped fiber Bragg grating (CFBG) fiber-optic sensors and their applications," *Sensors*, vol. 18, no. 7, p. 2147, Jul. 2018.

[17] C. A. F. Marques, P. Antunes, P. Mergo, D. J. Webb, and P. Andre, "Chirped Bragg gratings in PMMA step-index polymer optical fiber," *IEEE Photon. Technol. Lett.*, vol. 29, no. 6, pp. 500–503, Mar. 15, 2017.

[18] S. Korganbayev, R. Min, M. Jelbuldina, X. Hu, C. Caucheteur, O. Bang, B. Ortega, C. Marques, and D. Tosi, "Thermal profile detection through high-sensitivity fiber optic chirped Bragg grating on microstructured PMMA fiber," *J. Lightw. Technol.*, vol. 36, no. 20, pp. 4723–4729, Oct. 15, 2018.

[19] E. Vorathin, Z. M. Hafizi, A. M. Aizzuddin, M. K. A. Zaini, and K. S. Lim, "A novel temperature-insensitive hydrostatic liquid-level sensor using chirped FBG," *IEEE Sensors J.*, vol. 19, no. 1, pp. 157–162, Jan. 2019.

[20] Y. Luo, B. Yan, Q. Zhang, G.-D. Peng, J. Wen, and J. Zhang, "Fabrication of polymer optical fibre (POF) gratings," *Sensors*, vol. 17, no. 3, p. 511, Mar. 2017.

[21] K. Peters, "Polymer optical fiber sensors—A review," *Smart Mater. Struct.*, vol. 20, no. 1, 2011, Art. no. 013002.

[22] A. Leal-Junior, A. Theodosiou, A. Frizera-Neto, M. J. Pontes, E. Shafir, O. Palchik, N. Tal, S. Zilberman, G. Berkovic, P. Antunes, P. André, K. Kalli, and C. Marques, "Characterization of a new polymer optical fiber with enhanced sensing capabilities using a Bragg grating," *Opt. Lett.*, vol. 43, no. 19, p. 4799, Oct. 2018.

[23] Y. Koike and M. Asai, "The future of plastic optical fiber," *NPG Asia Mater.*, vol. 1, no. 1, pp. 22–28, Oct. 2009.

[24] A. Theodosiou, A. Lacraz, A. Stassis, C. Koutsides, M. Komodromos, and K. Kalli, "Plane-by-plane femtosecond laser inscription method for single-peak Bragg gratings in multimode CYTOP polymer optical fiber," *J. Lightw. Technol.*, vol. 35, no. 24, pp. 5404–5410, Dec. 15, 2017.

[25] A. Lacraz, K. Kalli, and A. Theodosiou, "Femtosecond laser inscribed Bragg grating arrays in long lengths of polymer optical fibres; a route to practical sensing with POF," *Electron. Lett.*, vol. 52, no. 19, pp. 1626–1627, Sep. 2016.

[26] A. Theodosiou, M. Komodromos, and K. Kalli, "Carbon cantilever beam health inspection using a polymer fiber Bragg grating array," *J. Lightw. Technol.*, vol. 36, no. 4, pp. 986–992, Feb. 15, 2018.

[27] A. Theodosiou, X. Hu, C. Caucheteur, and K. Kalli, "Bragg gratings and Fabry-Perot cavities in low-loss multimode CYTOP polymer fiber," *IEEE Photon. Technol. Lett.*, vol. 30, no. 9, pp. 857–860, May 1, 2018.

[28] T. Li, C. Shi, Y. Tan, R. Li, Z. Zhou, and H. Ren, "A diaphragm type fiber Bragg grating vibration sensor based on transverse property of optical fiber with temperature compensation," *IEEE Sensors J.*, vol. 17, no. 4, pp. 1021–1029, Feb. 2017.

[29] T. Li, Y. Tan, X. Han, K. Zheng, and Z. Zhou, "Diaphragm based fiber Bragg grating acceleration sensor with temperature compensation," *Sensors*, vol. 17, no. 12, p. 218, Jan. 2017.

[30] M. F. Domingues, N. Alberto, C. S. J. Leitao, C. Tavares, E. R. De Lima, A. Radwan, V. Sucasas, J. Rodriguez, P. S. B. Andre, and P. F. C. Antunes, "Insole optical fiber sensor architecture for remote gait analysis—An e-Health solution," *IEEE Internet Things J.*, vol. 6, no. 1, pp. 207–214, Feb. 2019.

[31] R. Li, "A diaphragm-type highly sensitive fiber Bragg grating force transducer with temperature compensation," *IEEE Sensors J.*, vol. 18, no. 3, pp. 1073–1080, Dec. 2018.

[32] C. A. F. Marques, G.-D. Peng, and D. J. Webb, "Highly sensitive liquid level monitoring system utilizing polymer fiber Bragg gratings," *Opt. Express*, vol. 23, no. 5, p. 6058, Mar. 2015.

[33] C. A. R. Diaz, A. G. Leal-Junior, P. S. B. Andre, P. F. D. C. Antunes, M. J. Pontes, A. Frizera-Neto, and M. R. N. Ribeiro, "Liquid level measurement based on FBG-embedded diaphragms with temperature compensation," *IEEE Sensors J.*, vol. 18, no. 1, pp. 193–200, Jan. 2018.

[34] A. Leal-Junior, A. Frizera, C. Díaz, C. Marques, M. Ribeiro, and M. J. Pontes, "Material features based compensation technique for the temperature effects in a polymer diaphragm-based FBG pressure sensor," *Opt. Express*, vol. 26, no. 16, p. 20590, Aug. 2018.

[35] J. Kennedy and R. Eberhart, "Particle swarm optimization," in *Proc. Int. Conf. Neural Netw. (ICNN)*, vol. 4, 1995, pp. 1942–1948.

[36] A. G. Leal-Junior, A. Frizera, C. R. Diaz, M. R. N. Ribeiro, and M. J. Pontes, "FBG-embedded oblong diaphragms with extended dynamic range," *IEEE Sens. Lett.*, vol. 2, no. 2, pp. 1–4, Jun. 2018.